Design and performance of bending-magnet beamline BL02B at the SSRF

Xiangyu Meng,[a] Zhi Guo,[a]* Yong Wang,[a]* Hui Zhang,[b] Yong Han,[b] Gaofeng Zhao,[a] Zhi Liu[b] and Renzhong Tai[a]*

[a]Shanghai Institute of Applied Physics, Chinese Academy of Sciences, Zhangheng Road 239, Pudong District, Shanghai 201800, People's Republic of China, and [b]Shanghai Institute of Microsystem and Information Technology, Chinese Academy of Sciences, Changning Road 865, Shanghai 200050, People's Republic of China. *Correspondence e-mail: guozhi@sinap.ac.cn, wangyong@sinap.ac.cn, tairenzhong@sinap.ac.cn

The BL02B bending-magnet beamline at the Shanghai Synchrotron Radiation Facility (SSRF) has been constructed and is now operational for ambient-pressure photoelectron spectroscopy (APPES) and photon-in/photon-out spectroscopy (PIPOS) experimental use. Optical optimization was implemented for realization of high performance, e.g. photon flux, energy-resolving power and focus spot size. X-ray photoelectron spectroscopy experiments show that the energy range extends from 40 to 2000 eV. Argon, nitrogen and neon gas core-shell excitation spectra indicate energy-resolving powers of over 1.4×10^4 @ 244 eV, 1.0×10^4 @ 401 eV and 7.0×10^3 @ 867 eV, respectively. The measured photon flux is 1.3×10^{11} photons s^{-1} @ $E/\Delta E$ = 3700 at 244 eV at the expected sample position, for the SSRF electron energy of 3.5 GeV and electron current of 240 mA. The spot sizes are 177 µm × 23 µm and 150 µm × 46 µm at the APPES and PIPOS samples, respectively.

1. Introduction

High energy-resolving power and high photon flux are essential for study of the electronic structures of new energy-related environmentally friendly materials using ambient pressure photoelectron spectroscopy (APPES) and photon-in/photon-out spectroscopy (PIPOS) (Guo et al., 2017). The application of APPES can provide information about solid or liquid surfaces in the presence of gases under ambient conditions (Salmeron & Schlögl, 2008; Ogletree et al., 2009). When the kinetic energy of the electron is 100 eV, the photoelectron inelastic mean-free path in a gas with a pressure of 1 Torr is approximately only a millimetre. Therefore, a small X-ray spot with high brightness is necessary for obtaining a high signal-to-noise ratio (Liu et al., 2014). High energy resolution is important for the APPES technique (Zhang et al., 2010; Blomberg et al., 2013), which can be used to study the active adsorption site, formation of a new chemical phase, and possible surface reconstruction. PIPOS includes soft X-ray absorption spectroscopy (XAS), soft X-ray emission spectroscopy (XES) and resonant inelastic X-ray scattering (RIXS). These techniques also require a high energy resolution and high photon flux to provide detailed information for both occupied and unoccupied electron states in the vicinity of the Fermi level (Himpsel, 2011).

In most cases, radiation with high brightness, photon flux and coherence is generated using undulators, which can be regarded as scarce and expensive sources (Feser et al., 2012). The number of bending magnets used at the Shanghai Synchrotron Radiation Facility (SSRF) is 40, which is twice as many as that of insertion devices. Therefore, it is crucial to

543
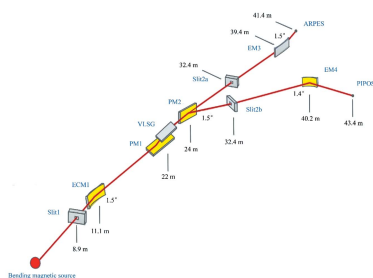
utilize bending magnets to tap the potential of synchrotron radiation. A large acceptance for the divergence angle should be implemented to acquire a relatively high photon flux. However, the large divergence angle leads to great aberration and, thus, a decreased energy resolution as well. The beamline design shall be optimized to make a balance between the flux and the energy resolution. The pre-focusing mirror is located as close as possible to the source. To fulfil the requirement of a large acceptance angle, the length of the mirrors and gratings must be large. To prevent aberration, an elliptical cylinder mirror (ECM1) and two ellipsoidal mirrors (EM3 and EM4) are used. One can also limit the coma aberration by optimizing the variable-line-spacing gratings (VLSGs) and demagnification of the beamline.

Our experiments show that the BL02B beamline can cover the energy range 40–2000 eV with a photon flux of 1.3×10^{11} photons s^{-1} @ $E/\Delta E = 3700$ and an energy-resolving power of over 10^4 at 244 eV. The spot sizes on samples are 177 µm × 23 µm and 150 µm × 46 µm for APPES and PIPOS, respectively. These parameters satisfy the demands for high energy resolution and high flux in APPES and PIPOS experiments.

2. Beamline

2.1. Bending-magnet source

The SSRF is a third-generation synchrotron with an electron energy of 3.5 GeV and a low emittance of 3.9 nm rad. The BL02B source is located on a standard bending-magnet section with a magnetic field of 1.27 T and a bending radius of 9.17 m. The electron current is 300 mA. Due to incoherence from the different positions of the electron ring, within the photon energy from 30 eV to 2500 eV, the angular photon flux densities along the x-axis (horizon) and y-axis (vertical) can be observed to follow a homogeneous and Gaussian distribution in a certain region, respectively. The spot size (FWHM) and angular divergence (FWHM) in the vertical direction for the bending-magnet radiation is shown in Fig. 1. The spot size decreases from 25.9 µm @ 30 eV to 23.1 µm @ 2500 eV, while the angular divergence decreases from 1620 µrad @ 30 eV to 178 µrad @ 2500 eV.
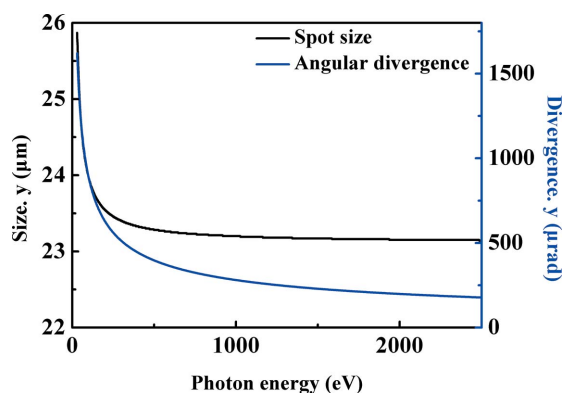

Figure 1
Source spot size and angular divergence in the vertical direction.

2.2. Beamline design

The BL02B beamline layout is shown in Fig. 2(a), with the main parameters for the beamline optics listed in Table 1. The lead-out angle for the front-end (the angle between the beam and the linear section of the storage ring) is 1°. A four-blade aperture (Slit1) is located 8.9 m downstream from the bending-magnet source, which can block undesirable photons and define the acceptance angle for the beamline. To obtain higher photon flux, a large horizontal divergence angle for the bending-magnet beamline is inevitable. Therefore, an elliptical cylinder mirror (ECM1) is located 11.1 m downstream from the source, which is as close as possible; moreover, the mirror length is over 1 m with a grazing-incident angle of 1.5° and a large acceptance angle of 2 mrad. ECM1 can horizontally focus the beam onto the exit slits located at 32.4 m. There are two exit slits in total: Slit2a for the APPES branch and Slit2b for the PIPOS branch, which are alternated by switching the plane mirror (PM2). The monochromator (Mono) is located at 22 m and consists of one internally water-cooled plane mirror (PM1) and three VLSGs. In addition to energy dispersion, the gratings can also vertically focus the beam onto the exit slit. To obtain high energy resolution and grating diffraction efficiency, three gratings are optimized for varying energy ranges. Gratings with line densities of 400 lines mm^{-1}, 800 lines mm^{-1} and 1100 lines mm^{-1} cover the energy ranges 40–600 eV, 200–1600 eV and 200–2000 eV, respectively. Due to the large vertical acceptance angle of 0.8 mrad, the −1st diffraction order and a C_{ff} (fixed focus constant) value of 0.6 is chosen for the whole energy range. Since the ECM1 and VLSG focus the beam onto the exit slit plane in the horizontal and vertical directions, respectively, the X-rays on the exit slit plane can be observed as a second source for the downstream ellipsoidal mirrors (EM3 and EM4). The entrance and exit arm lengths are 7 m and 2 m for EM3, and 7.8 m and 3.2 m for EM4, respectively. The two mirrors can be used to focus the beam onto the sample positions for APPES (41.4 m) and PIPOS (43.4 m).

3. Beamline design specifications

3.1. Energy resolution

The monochromator is designed to correct optical aberrations using the light-path function method (Harada & Kita, 1980; Kiyokura *et al.*, 1998). Due to the fixed exit slit, optical aberrations degrade the energy resolution of the grating. The main optical aberrations (Itou *et al.*, 1989; Reininger, 2011; Xue *et al.*, 2014) can be minimized using a line density variation on the grating given by

$$k(w) = k_0\big(1 + 2b_2w + 3b_3w^2 + 4b_4w^3\big), \tag{1}$$

where k_0 is the line density at the grating centre, w is the coordinate along the grating length and b_2, b_3 and b_4 are the varied-line-spacing parameters used to defocus the monochromatic beam, correct the coma aberration and spherical aberration, respectively. The defocus term for the light-path function can be expressed as

Table 1
Parameters for the beamline optics.

| Element	Position (m)	Shape	Optical area (L × W) (mm)	Deflection/angle (°)	Coating	Slope error (tangential/sagittal) (µrad)	Roughness (nm)
Slit1	8.9	–	–	–	–	–	–
ECM1	11.1	Elliptical cylindrical	980 × 40	1.5	Au	0.75/5	0.4
PM1	22	Plane	340 × 30	Variable	Au	0.2/2.5	0.6
VLSG	22	Plane	170 × 30	Variable	Au	0.12/2	0.5
PM2	24	Plane	380 × 30	1.5	Au	0.4/2.3	0.3
Slit2a	32.4	–	–	–	–	–	–
EM3	39.4	Ellipsoidal	340 × 15	1.5	Au	1/5	0.7
APPES	41.4	–	–	–	–	–	–
Slit2b	32.4	–	–	–	–	–	–
EM4	40.2	Ellipsoidal	360 × 15	1.4	Au	1/5	0.5
PIPOS	43.4	–	–	–	–	–	–
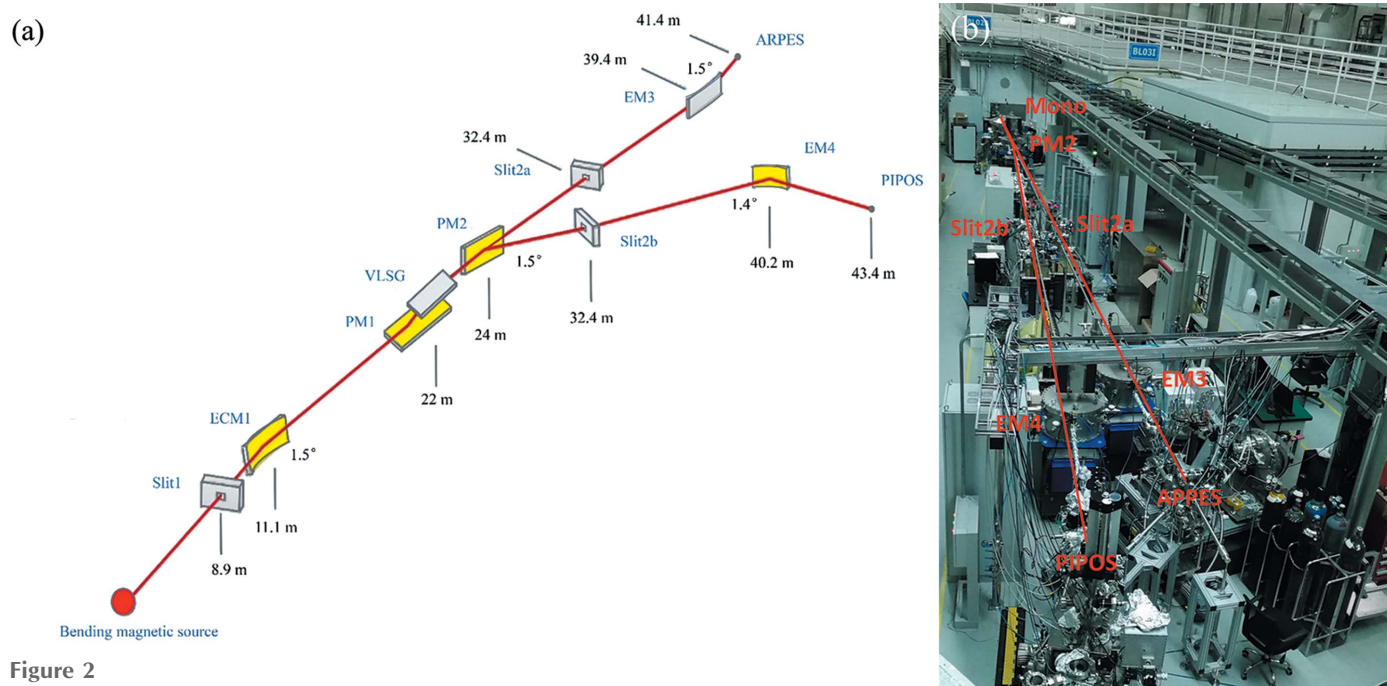
Figure 2
(a) Optical layout and (b) photograph of the BL02B beamline.

$$F_{20} = \frac{\cos^2 \alpha}{r_1} + \frac{\cos^2 \beta}{r_2} - 2b_2 n k_0 \lambda, \tag{2}$$

where α and β are the incidence and diffraction angles, respectively, r_1 is the entrance arm length, r_2 is the exit arm length, n is the diffraction order and λ is the wavelength. F_{20} can be zeroed within the whole energy range using a suitable choice of b_2 to simultaneously solve the grating equation and equation (2). This yields a unique pair of angles α and β for each photon energy and grating. The coma term is the primary aberration and can be expressed as

$$F_{30} = \sin \alpha \frac{\cos^2 \alpha}{r_1^2} + \sin \beta \frac{\cos^2 \beta}{r_2^2} - 2b_3 n k_0 \lambda. \tag{3}$$

At a certain energy, F_{30} is zero; for the whole energy range covered by each grating, the effect of the coma aberration can be negligible due to its weak value.

Five factors contribute to the energy resolution, including the source size ΔE_{so}, exit slit size ΔE_{ex}, tangential slope error for the grating ΔE_{gr} and plane mirror ΔE_{pl}, and the aberration of the beamline ΔE_{ab}. The total energy resolution can be expressed as

$$\Delta E_{total} = \left(\Delta E_{so}^2 + \Delta E_{ex}^2 + \Delta E_{gr}^2 + \Delta E_{pl}^2 + \Delta E_{ab}^2 \right)^{1/2}. \tag{4}$$

The slope errors for the plane mirror and gratings are 0.2 µrad and 0.12 µrad in the meridional direction, respectively. When the exit slit size is chosen to be 15 µm, the resolving powers for each grating are calculated as shown in Fig. 3(a). The contributions to the energy broadening ΔE_{total} are the source size, exit slit size, slope error of the plane mirror and grating and beamline aberration in sequence. As seen in the figure, the resolving power decreases with increasing energy. At energies up to 2500 eV, the resolving power remains greater than 3500. The resolution can be verified using a ray-tracing model called
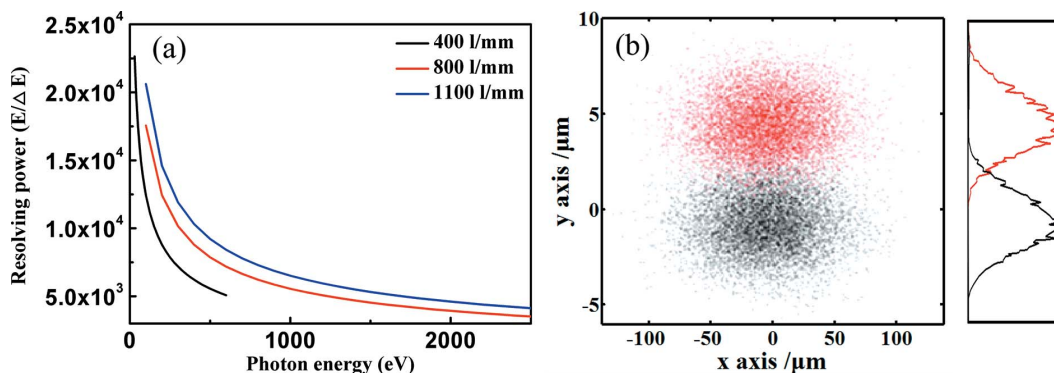
Figure 3
(*a*) Resolving power as a function of energy for different gratings, 400 lines mm^{-1}, 800 lines mm^{-1} and 1100 lines mm^{-1}. (*b*) Spot patterns at the exit plane for 250 eV and 250.018 eV with 1100 lines mm^{-1} grating.

the *SHADOW* code (Tanaka & Kitamura, 2001). As an example, we show the spot patterns obtained at the exit plane for 250 eV and 250.018 eV with an 1100 lines mm^{-1} grating in Fig. 3(*b*). The two patterns can be well separated, which indicates a resolving power of 14000. Under this condition, the resolving power is 13200 in Fig. 3(*a*), which is slightly worse due to the contribution of the 15 μm exit slit.

3.2. Photon flux

The photon flux at the sample can be calculated by considering the angular divergence limited by Slit1 and the transmission efficiencies for the mirrors and gratings. The vertical divergence for Slit1 is modified according to variation in photon energy. Due to the finite length of ECM1, the divergence in the horizontal direction should be limited to 2 mrad. The surface roughness of all the optical elements is listed in Table 1. The efficiency of the grating depends on the grating duty ratio, line density and groove depth. Neviere's code is used to optimize the grating parameters and obtain the maximum efficiencies for the gratings (Nevière *et al.*, 1974).

The photon flux for varying vertical divergence is shown in Fig. 4. For the 400 lines mm^{-1}, 800 lines mm^{-1} and 1100 lines mm^{-1} gratings, the photon flux at the PIPOS sample is lower than that obtained at the APPES sample, since an additional switching mirror is used at the PIPOS branch. For the

400 lines mm^{-1} grating, the maximum flux @ 150 eV is higher than 1.3×10^{12} photons s^{-1}. For the 800 lines mm^{-1} and 1100 lines mm^{-1} gratings, the flux is approximately flat at low and moderate energy and decreases rapidly at high energy.

3.3. Spot size at the sample

A small spot with high flux density at the endstation is required for the APPES and PIPOS experiments. The ellipsoidal mirror can reduce the reflection losses compared with the Kirkpatrick–Baez pair. Therefore, two ellipsoidal mirrors are chosen to focus the beam onto the sample positions for APPES and PIPOS. To decrease the spot size, the demagnification ratio for the mirror is up to 3.5:1, with slope errors of 1 μrad × 5 μrad for both mirrors. The spot sizes at the samples with an exit slit of 35 μm are simulated using ray tracing, as shown in Fig. 5. The spot sizes at the APPES and PIPOS samples are 111 μm × 13.5 μm (FWHM) at 800 eV and 133 μm × 10 μm (FWHM) at 400 eV, respectively.

4. Experimental results

4.1. Energy resolution

An ionization chamber was installed downstream of the exit slit to measure the core-shell excitation spectra for several gases, from which we can obtain the energy resolution. A microchannel plate (MCP) was mounted on the chamber to record the total ion yield spectra. The ionization chamber includes a vacuum system, gas inlet system, detection system and data acquisition and processing system. The advantage of using the ionization chamber is that the gas core-shell ionization spectra can be measured under a very low working pressure so that collision broadening becomes negligible. In our experiments, the spectra were recorded for a gas pressure of 10^{-6} Torr with an exit slit opening of 15 μm. The measured spectrum was a
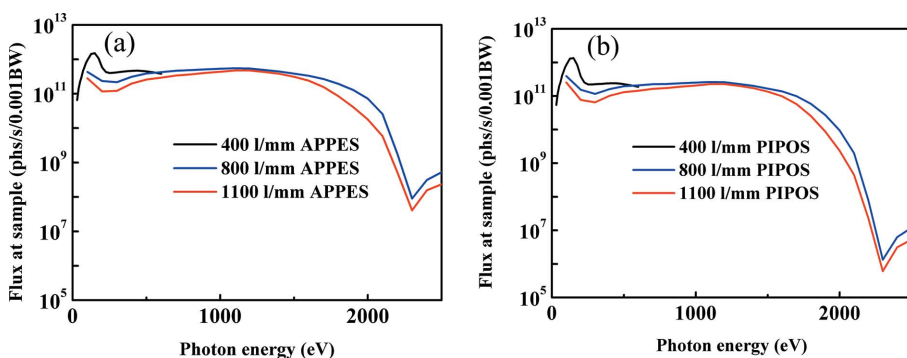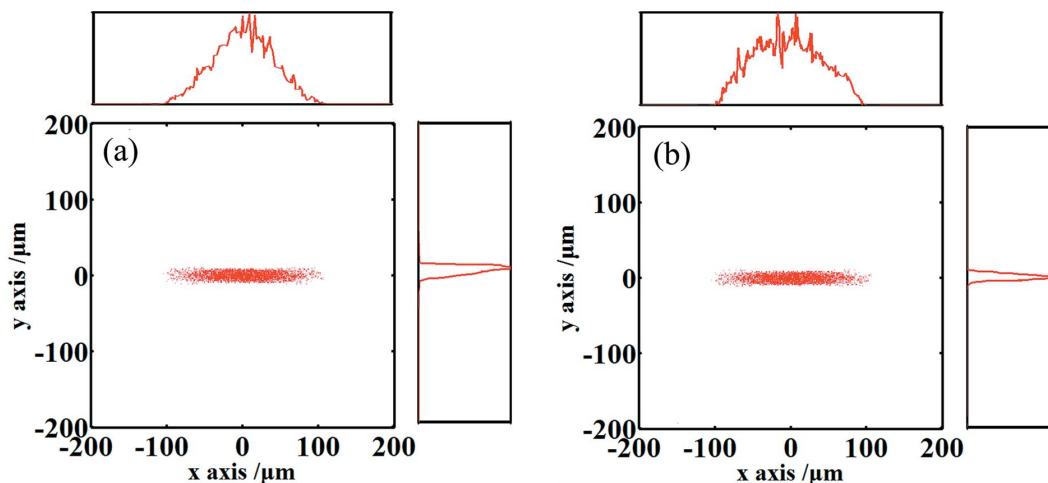

Figure 4
Photon flux at the (*a*) APPES sample and (*b*) PIPOS sample as a function of energy for different gratings.

Figure 5
(*a*) Spot size at the APPES sample for 800 eV with a 35 µm exit slit. (*b*) Spot size at the PIPOS sample for 400 eV with a 35 µm exit slit.

Voigt profile: a convolution of a naturally broadened Lorentzian ΔL with an instrumental Gaussian width Γ_G.

Fig. 6(*a*) shows the core-shell excitation spectra for Ar obtained using the 1100 lines mm^{-1} grating. The Ar $L_{2,3}$ absorption-edge transitions to the Rydberg levels $2p_{3/2} \rightarrow 4s$, $3d$, $4d$, $5d$, $6d$, $7d$ and $2p_{1/2} \rightarrow 4s$, $3d$, $4d$, $5d$, $6d$ were all observed (King *et al.*, 1977; Xue *et al.*, 2010). The $2p_{3/2} \rightarrow 4s$ transition ($h\nu = 244.39$ eV) was used to characterize the energy resolution. Assuming a Lorentzian linewidth $\Delta L = 112$ meV (Prince *et al.*, 1999; Strocov *et al.*, 2010), we obtained a Gaussian width of $\Gamma_G = 17$ meV $\pm$ 2 meV and a resolving power of 1.4×10^4, which can be compared with a theoretical resolving power of 1.3×10^4.

Fig. 6(*b*) shows the spectra measured for N_2 (dotted line) in the range of the N $1s \rightarrow \pi^*$ excitation (Sodhi & Brion, 1984). Six transition energies from N $1s$ ($\nu = 0$) $\rightarrow \pi^*$ ($\nu':\nu' = 0$–5) were clearly observed. By fitting the experiment spectra with a Voigt linewidth $\Delta L = 113$ meV, we obtained a Gaussian width of $\Gamma_G = 39$ meV $\pm$ 1 meV and a resolving power of 1.0×10^4, which can be compared with the theoretical value of 1.1×10^4.

Fig. 6(*c*) shows the spectrum for Ne at the $1s$ Rydberg series measured with the 1100 lines mm^{-1} grating. The fine structure resonances $1s \rightarrow 3p$ ($h\nu = 867.1$ eV), $4p$, $5p$ and $6p$ were all clearly observed. To estimate the resolution, we fitted the Ne spectra with a Lorentzian linewidth of $\Delta L = 230$ meV (Gelius *et al.*, 1974). This yielded a Gaussian width of $\Gamma_G = 124$ meV $\pm$ 3 meV and a resolving power of 7.0×10^3, which again conformed well to the theoretical value of 7.2×10^3.

4.2. Flux at the sample

The photon flux at the expected APPES and PIPOS sample positions was measured within the whole energy range using an AXUV100G photodiode. The vertical divergence varies at different energies, with the energy resolution estimated from the gas core-shell excitation spectra measured in Section 4.1. For the Ar $L_{2,3}$ spectra at 244 eV, the experimental photon flux obtained for the 400 lines mm^{-1} grating at the APPES branch is 1.3×10^{11} photons s^{-1} @ $E/\Delta E = 3700$, while the theoretical

flux is calculated to be 4×10^{11} photons s^{-1} (0.1% bandwidth)$^{-1}$ (*cf*. Fig. 4). Fig. 7 shows the photon flux at the APPES and PIPOS expected sample positions as a function of energy. The maximum flux was 5×10^{11} photons s^{-1} (0.1% bandwidth)$^{-1}$ at 125 eV at the APPES expected sample position using the 400 lines mm^{-1} grating. The experimental flux coincides with the theoretical results in Fig. 4. The dip in the photon flux at approximately 285 eV originated from carbon contamination of the beamline optics (mirrors and gratings). *In situ* synchrotron-radiation-activated oxygen cleaning is now operational for the removal of such contamination (Warburton & Pianetta, 1992).

4.3. Energy range

According to the photoelectron spectroscopy principle,

$$\mathrm{KE} = h\nu - \mathrm{BE} - \Phi, \tag{5}$$

where BE is the binding energy of the atomic orbitals from which the electron originates, $h\nu$ is the photon energy, KE is the kinetic energy of the emitted electron measured by the instrument and Φ is the work function of the spectrometer. A VG Scienta Hipp3 analyzer was used to carry out X-ray photoelectron spectroscopy (XPS) experiments and obtain the kinetic energy. The work function for the spectrometer was 4.3 eV and the pass energy was set to be 50 eV. By analyzing the kinetic energy of an electron from a typical atomic orbital, we can obtain the photon energy. The valence band (VB)-XPS for an Ag film sample at the APPES endstation was measured by the electron energy analyzer, as shown in Fig. 8(*a*). A KE(E_F) value (dashed line) of 35.6 eV was obtained from VB-XPS for the Ag film. Because the Ag BE is 0 eV, the photon energy was deduced to be 39.9 eV. In addition, Ag $3d$ XPS was also measured, as shown in Fig. 8(*b*). The kinetic energy obtained from the XPS profile and binding energy for Ag $3d_{5/2}$ obtained from a database (Moulder *et al.*, 1995) was 1639.8 eV and 368.3 eV, respectively. According to equation (5), we calculate the photon energy to be $h\nu = 2014.04$ eV. By
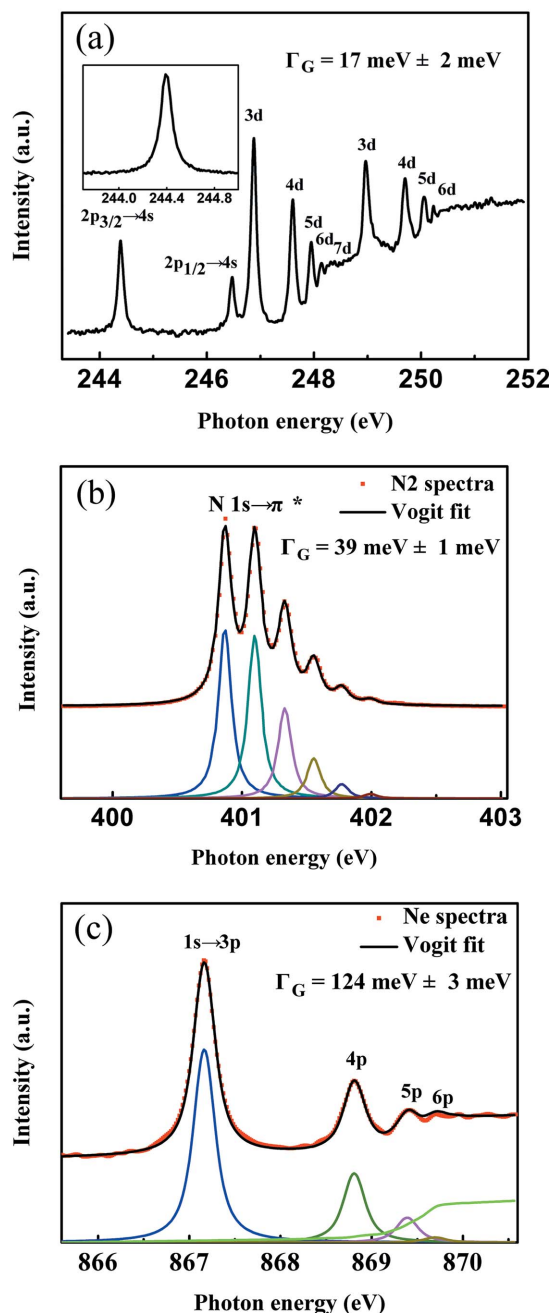
Figure 6
Ion yield spectra measured with the 1100 lines mm^{-1} grating. The opening for the exit slit is 15 µm. (a) Excitation spectra for Ar gas at the Ar L-edge from 244 eV to 251 eV. The resolving power is 1.4×10^4, as calculated from the $2p_{3/2} \rightarrow 4s$ transition. (b) Excitation spectra for N$_2$ gas at the N K-edge around the energy 401 eV. The resolving power is 1.0×10^4, as calculated from peak fitting. (c) Excitation spectra for Ne gas at the Ne K-edge from 866 eV to 870 eV. The resolving power is 7.0×10^3, as calculated from peak fitting.
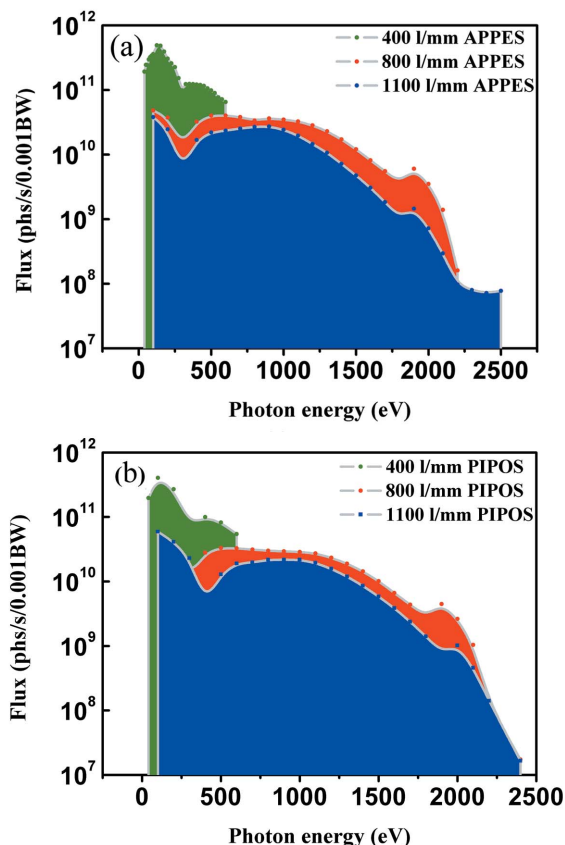

Figure 7
Photon flux at the APPES and PIPOS expected sample positions as a function of energy for different gratings.

YAG:Ce scintillator, NAVITAR zoom lens system and CCD camera. The scintillator is 50 µm thick, which generates visible light at X-ray radiation illumination. The zoom lens offers 0.58× to 7× magnification in the detector system. The CCD camera, with a pixel size of 13.5 µm, is used to detect visible light. The spot size at the sample was measured using a vertical exit slit of 35 µm. Fig. 9 shows that the spot sizes are 177 µm × 23 µm and 150 µm × 46 µm at the APPES and PIPOS samples, respectively.

5. APPES and PIPOS endstations

The APPES endstation contains a fast-access load lock, a sample preparation chamber, an analysis chamber and an energy analyzer. The load lock chamber can be evacuated to 10^{-7} mbar within an hour, which facilitates fast sample transfers. The sample preparation chamber has an ion gun for sputtering and a low-energy electron diffraction (LEED) setup for surface structure characterization. The X-rays are let into the analysis chamber through a thin Si$_3$N$_4$ membrane that provides pressure isolation. Through a pre-lens, the analysis chamber is connected to the VG Scienta Hipp3 energy analyzer, which is designed for measurements of photoelectron spectroscopy under ambient-pressure conditions ranging from ultrahigh-vacuum (UHV) to 20 mbar. The ion gauge and capacitance diaphragm gauge are mounted on the analysis
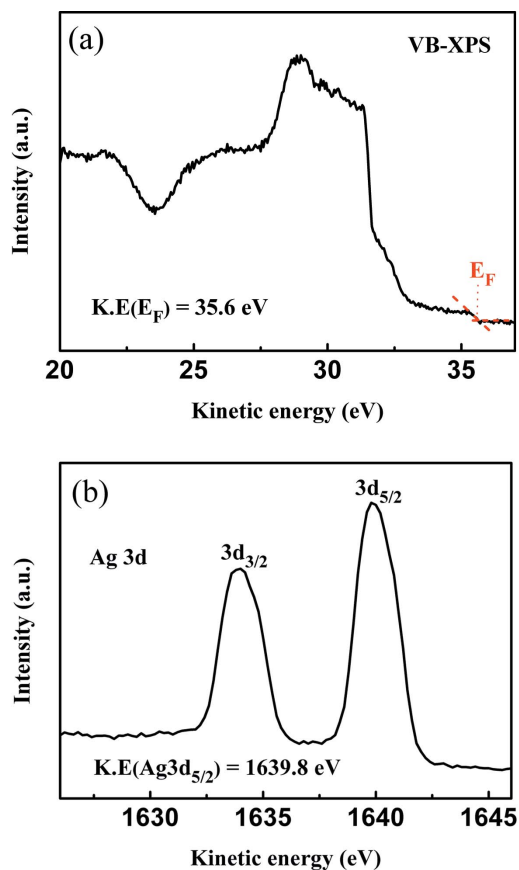
measuring the Ag photoelectron spectrum, the beamline energy range was found to range from 39.9 eV to 2014.04 eV.

4.4. Spot size at the sample

A high-resolution imaging system was installed at the endstation to measure the spot size. This system consisted of a

Figure 8
(a) Valence band (VB) XPS and (b) Ag 3d XPS for the Ag film. The dashed line shows the kinetic energy value for the Fermi level.

Figure 9
Spot size at (a) the APPES sample and (b) the PIPOS sample, which are 177 µm × 23 µm and 150 × 46 µm, respectively.

chamber to monitor the gas pressure ranging from 10^{-10} mbar to 10^{-4} mbar and from 10^{-4} mbar to 100 mbar, respectively. Besides, the second differential pumping stage is equipped with a quadrupole mass spectrometer that could monitor the reaction gases. We briefly present some results carried out at the APPES endstation. The sample is 100 nm Au film deposited on Si wafer. The pre-lens of the energy analyzer is 0.3 mm distance from the Au film surface. The photon energy and the pass energy for the energy analyzer are chosen to be 500 eV and 50 eV, respectively. Fig. 10(a) shows the Au 4f XPS spectrum under the UHV pressure and with 1.27 mbar N_2. Due to the strong scattering of photoelectrons, the spectrum intensity decreases with the N_2 pressure increasing.

The PIPOS endstation contains a fast-access load lock, a transfer chamber, a sample preparation chamber and an analysis chamber. The sample surface can be cleaned by argon-ion etching and vacuum annealing on the sample preparation chamber. Furthermore, the film can be grown using the MBE method with different oxygen pressures and its surface orientation can be in situ detected by the LEED setup. The analysis chamber includes low-temperature and a high-temperature sample stages, where the absorption spectra can be measured with the temperature ranging from 70 K to 600 K. Besides, in situ charge–discharge experiments for energy materials can be carried out under the UHV and ambient pressure conditions by using the in situ reaction
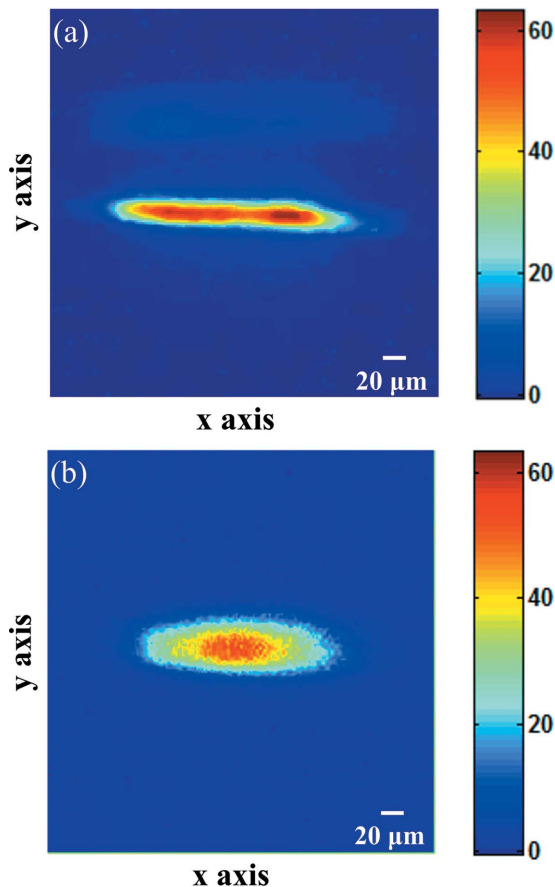
device. The X-ray absorption spectra can be collected in both total electron yield and total fluorescence yield modes simultaneously with a base pressure of approximately 5×10^{-10} Torr. The photon energy can be calibrated with the spectra of the reference samples (CoO, MnO, NiO and SrTiO3), which are measured simultaneously. The X-ray absorption spectra of graphite film are measured using the the total electron yield technique at the PIPOS endstation. Fig. 10(b) shows C K-edge XANES with different X-ray incident angle. Two small peaks are observed near 286.7 eV and 290.3 eV with the angle of 75°. With the angle decreasing, these two peaks weaken gradually, and disappear at the normal incident angle of 0°.

6. Conclusion

The BL02B bending-magnet beamline at the SSRF for high energy resolution and high flux has been constructed. To realize high performance, the beamline was optimized by using an elliptical cylinder mirror as the first mirror, three gratings covering different energy ranges, and high demagnification ratio (>3:1) ellipsoidal mirrors. The measured photon flux at the APPES sample at 244 eV is 1.3×10^{11} photons s^{-1} @ $E/\Delta E$ = 3700. The energy-resolving powers are measured to be over 10000 at 244 eV and 401 eV, which coincide with the
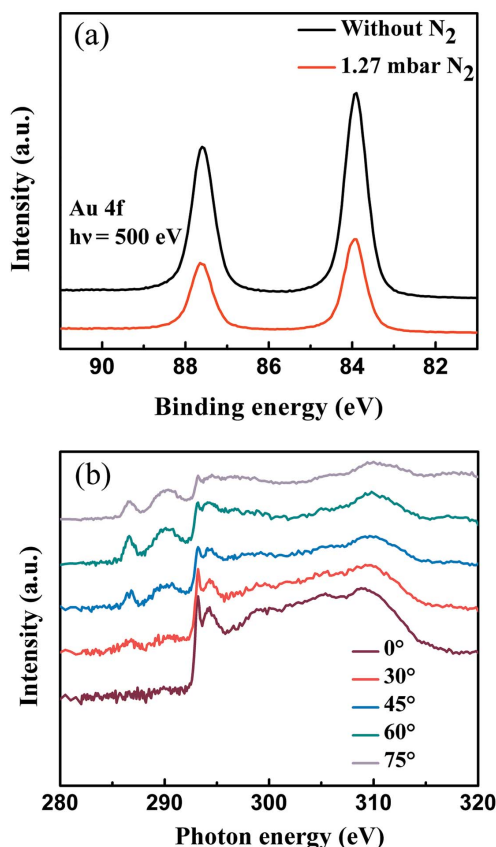
Figure 10
(a) Au 4f XPS spectrum with N_2 and without N_2 at the APPES endstation. (b) C K-edge XANES of graphite film with different X-ray incident angle using the total electron yield technique. The angle is between the incident X-ray and the normal direction.

design values. The spot sizes at the APPES and the PIPOS samples are 177 μm × 23 μm and 150 μm × 46 μm, respectively. Due to the high performance within a wide energy range from 40 eV to 2000 eV, the BL02B beamline can be utilized to carry out novel APPES and PIPOS experiments. The APPES and PIPOS endstations have been built up and can offer a platform for study of electronic structures under UHV and ambient pressure conditions.

References

Blomberg, S., Hoffmann, M. J., Gustafson, J., Martin, N. M., Fernandes, V. R., Borg, A., Liu, Z., Chang, R., Matera, S., Reuter, K. & Lundgren, E. (2013). *Phys. Rev. Lett.* **110**, 117601.

Feser, M., Howells, M. R., Kirz, J., Rudati, J. & Yun, W. (2012). *J. Synchrotron Rad.* **19**, 751–758.

Gelius, U., Svensson, S., Siegbahn, H., Basilier, E., Faxälv, A. & Siegbahn, K. (1974). *Chem. Phys. Lett.* **28**, 1–7.

Guo, Z., Meng, X., Wang, Y., Liu, H., Zhang, X., Li, Z., Xue, L. & Tai, R. (2017). *J. Synchrotron Rad.* **24**, 877–885.

Harada, T. & Kita, T. (1980). *Appl. Opt.* **19**, 3987–3993.

Himpsel, F. (2011). *Phys. Status Solidi B*, **248**, 292–298.

Itou, M., Harada, T. & Kita, T. (1989). *Appl. Opt.* **28**, 146–153.

King, G. C., Tronc, M., Read, F. H. & Bradford, R. C. (1977). *J. Phys. B: At. Mol. Phys.* **10**, 2479–2495.

Kiyokura, T., Maeda, F. & Watanabe, Y. (1998). *J. Synchrotron Rad.* **5**, 572–574.

Liu, X. S., Yang, W. L. & Liu, Z. (2014). *Adv. Mater.* **26**, 7710–7729.

Moulder, J., Chastain, J. & King, R. (1995). *Handbook of X-ray Photoelectron Spectroscopy: A Reference Book of Standard Spectra for Identification and Interpretation of XPS Data.* Eden Prairie: Perkin-Elmer Corporation.

Nevière, M., Vincent, P. & Petit, R. (1974). *Nouv. Rev. Opt.* **5**, 65.

Ogletree, D. F., Bluhm, H., Hebenstreit, E. D. & Salmeron, M. (2009). *Nucl. Instrum. Methods Phys. Res. A*, **601**, 151–160.

Prince, K., Vondráček, M., Karvonen, J., Coreno, M., Camilloni, R., Avaldi, L. & de Simone, M. (1999). *J. Electron Spectrosc. Relat. Phenom.* **101–103**, 141–147.

Reininger, R. (2011). *Nucl. Instrum. Methods Phys. Res. A*, **649**, 139–143.

Salmeron, M. & Schlögl, R. (2008). *Surf. Sci. Rep.* **63**, 169–199.

Sodhi, R. N. & Brion, C. (1984). *J. Electron Spectrosc. Relat. Phenom.* **34**, 363–372.

Strocov, V. N., Schmitt, T., Flechsig, U., Schmidt, T., Imhof, A., Chen, Q., Raabe, J., Betemps, R., Zimoch, D., Krempasky, J., Wang, X., Grioni, M., Piazzalunga, A. & Patthey, L. (2010). *J. Synchrotron Rad.* **17**, 631–643.

Tanaka, T. & Kitamura, H. (2001). *J. Synchrotron Rad.* **8**, 1221–1228.

Warburton, W. K. & Pianetta, P. (1992). *Nucl. Instrum. Methods Phys. Res. A*, **319**, 240–243.

Xue, C., Wang, Y., Guo, Z., Wu, Y., Zhen, X., Chen, M., Chen, J., Xue, S., Peng, Z., Lu, Q. & Tai, R. (2010). *Rev. Sci. Instrum.* **81**, 103502.

Xue, L., Reininger, R., Wu, Y.-Q., Zou, Y., Xu, Z.-M., Shi, Y.-B., Dong, J., Ding, H., Sun, J.-L., Guo, F.-Z., Wang, Y. & Tai, R.-Z. (2014). *J. Synchrotron Rad.* **21**, 273–279.

Zhang, C. J., Grass, M. E., McDaniel, A. H., DeCaluwe, S. C., El Gabaly, F., Liu, Z., McCarty, K. F., Farrow, R. L., Linne, M. A., Hussain, Z., Jackson, G. S., Bluhm, H. & Eichhorn, B. W. (2010). *Nat. Mater.* **9**, 944–949.